

Topological phononics arising from fluid-solid interactions

Received: 24 March 2022

Accepted: 6 October 2022

Published online: 17 October 2022

 Check for updatesXiaoxiao Wu^{1,2,7}, Haiyan Fan^{3,7}, Tuo Liu⁴, Zhongming Gu⁵,
Ruo-Yang Zhang⁶, Jie Zhu⁵✉ & Xiang Zhang¹✉

Nontrivial band topologies have been discovered in classical systems and hold great potential for device applications. Unlike photons, sound has fundamentally different dynamics and symmetries in fluids and solids, represented as scalar and vector fields, respectively. So far, searches for topological phononic materials have only concerned sound in either fluids or solids alone, overlooking their intricate interactions in “mixtures”. Here, we report an approach for topological phononics employing such unique interplay, and demonstrate the realization of type-II nodal rings, elusive in phononics, in a simple three-dimensional phononic crystal. Type-II nodal rings, as line degeneracies in momentum space with exotic properties from strong tilting, are directly observed through ultrasonic near-field scanning. Strongly tilted drumhead surface states, the hallmark phenomena, are also experimentally demonstrated. This phononic approach opens a door to explore topological physics in classical systems, which is easy to implement that can be used for designing high-performance acoustic devices.

Nontrivial band topologies, stemming from nodal points of quantum condensed matters where energy bands intersect each other in the reciprocal space^{1,2}, have been discovered in photonic and phononic systems^{3,4}. Manifested by exotic transport of photons^{5,6} and sound waves^{7–9}, they hold great potential for applications^{10–20} such as lasing^{15,16}, sensing^{17,18}, and energy harvesting^{19,20}. Due to their close relationship, searches for topological phononic systems are often inspired by the counterparts in photonics⁴ and only concern sound in either fluids or solids alone. As a mechanical wave²¹, sound propagates as a perturbation of density in fluids and elastic displacements in solids, and it is hence represented by a scalar field and vector field, respectively. This fundamental point leads to intrinsic differences in the dynamics and symmetries for sound in fluids and solids, a characteristic absent in photonics²². However, such intrinsic differences and their possible interactions have yet to be considered in the

development of topological phononics, even for the underwater environment where the interactions can become considerable^{23,24}.

In fact, among the band topologies besides touching at a single point, which forms a Dirac node²⁵ or Weyl node²⁶, the nodal points can also form line degeneracies along a closed loop, so-called nodal lines^{27,28}, with geometric configurations such as nodal rings²⁹, nodal chains³⁰ and nodal links³¹. Originally perceived to be mimicking high-energy particles dictated by Lorentz invariance, however, an extra tilting can exist for the nodal points in the bands of periodic systems³². When the tilting becomes strong enough such that it cannot be adiabatically removed³³, unconventional type-II Dirac points^{14,34}, Weyl points^{35,36}, and nodal rings^{37,38} arise, distinguished by finite density of states at the node energy and strong anisotropic transport properties compared with their type-I counterparts^{39–41}. To date, there is still no realization for type-II nodal rings in phononics, which seems to require

¹Faculties of Sciences and Engineering, The University of Hong Kong, Hong Kong, China. ²Quantum Science and Technology Center and Advanced Materials Thrust, The Hong Kong University of Science and Technology (Guangzhou), Nansha, Guangzhou 511400 Guangdong, China. ³Department of Mechanical Engineering, The Hong Kong Polytechnic University, Hung Hom, Kowloon, Hong Kong, China. ⁴Key Laboratory of Noise and Vibration Research, Institute of Acoustics, Chinese Academy of Sciences, Beijing 100190, China. ⁵Institute of Acoustics, School of Physics Science and Engineering, Tongji University, Shanghai 200092, China. ⁶Department of Physics, The Hong Kong University of Science and Technology, Clear Water Bay, Kowloon, Hong Kong, China. ⁷These authors contributed equally: Xiaoxiao Wu, Haiyan Fan. ✉e-mail: jiezhu@tongji.edu.cn; president@hku.hk

more tortuous designs than already very complicated realizations of type-II Dirac or Weyl points using phononic crystals^{11,14}.

In this article, we propose and experimentally demonstrate type-II nodal rings for sound with a unique approach developed for topological phononics. The approach utilizes the different wave dynamics and symmetry representations of sound in fluids and solids, specifically, the interplay of the scalar nature of sound in fluids and its vectorial nature in solids, a feature absent for photons. With this approach, type-II nodal rings are realized in a simple three-dimensional (3D) phononic crystal, which is identical perforated metallic plates immersed in water. Arising from the interaction between waterborne sound and elastic modes of the solid plates, the type-II nodal rings are revealed through ultrasonic near-field scanning. Strongly tilted drumhead surface states (DSSs) stemming from the type-II nodal rings are also experimentally observed. Nodal chains also emerge in the simple structure. Our study demonstrates that the interaction in phononic crystals made of fluid-solid “mixtures” (unit cells comprising

both fluid and solid components), previously often disregarded for simplicity when searching topological materials in phononics, can lead to rich phenomena unattainable for solely fluid-borne or solid-borne sound. Thereby it provides a novel platform for exploring unique topological physics and acoustic applications.

Results

Type-II nodal rings arising from fluid-solid interactions

We start from considering a 3D phononic crystal immersed in a fluid (Fig. 1a). The phononic crystal comprises identical metallic plates separated by the fluid, each plate perforated with a square lattice of circular through holes. Here, we adopt aluminum and water for demonstration purpose. Water, unlike air, have comparable acoustic impedance with aluminum, substantially facilitating fluid-solid interaction. The first four bands of the phononic crystal originate from the three lowest plate modes and the waterborne sound. The calculated band structure (Fig. 1b) along the high-symmetry directions of the first

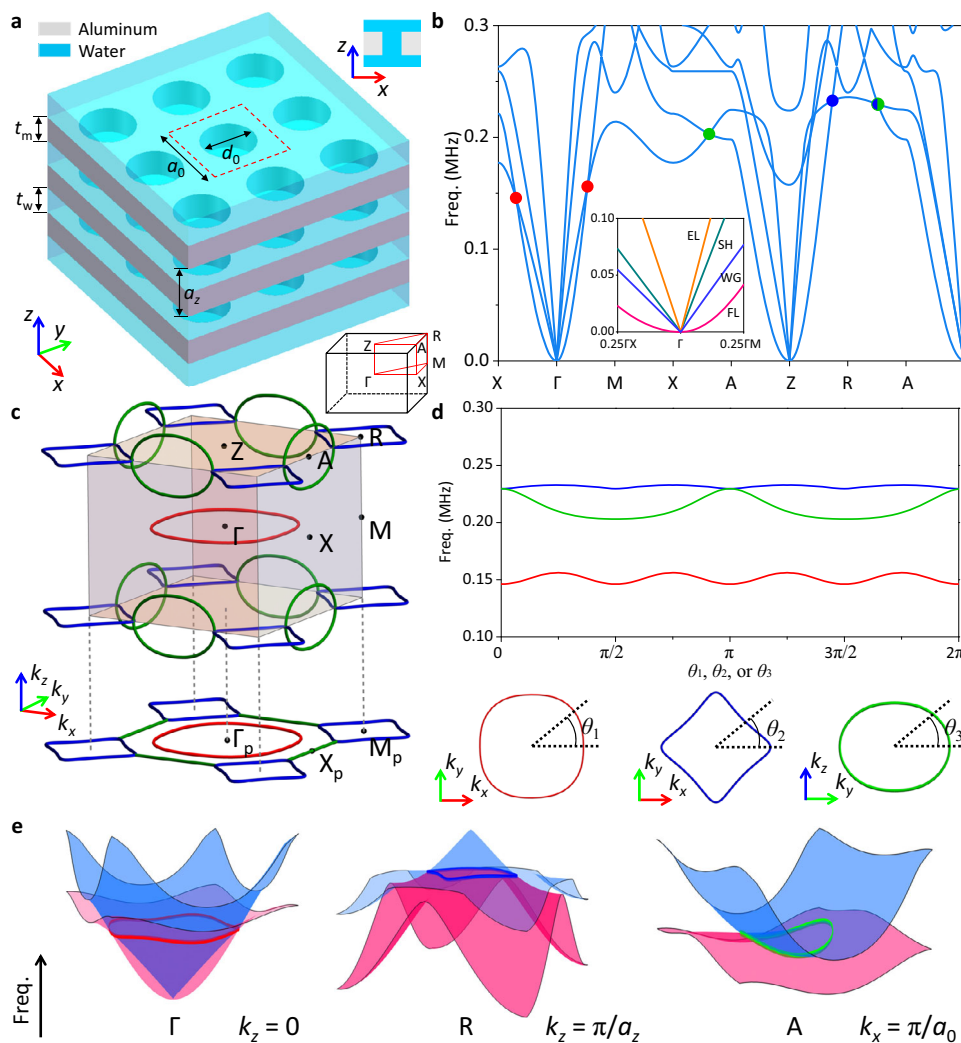


Fig. 1 | Type-II nodal rings induced by fluid-solid interaction. **a** Perspective and cross-sectional views of the 3D phononic crystal, formed with identical aluminum plates with circular through holes immersed in water. The phononic crystal belongs to the space group P4/mmm (No. 123). Inset: schematic of the first Brillouin zone (FBZ). The red dashed square indicates a single unit cell (z direction not shown). The in-plane lattice constant $a_0 = 3$ mm, the diameter of holes $d_0 = 2$ mm, the thickness of plates $t_m = 2$ mm, the separation of plates $t_w = 2$ mm, corresponding to out-of-plane lattice constant $a_z = t_m + t_w = 4$ mm. **b** Calculated band structure along high-symmetry directions in FBZ. The dots indicate the crossings of the 1st and 2nd

bands, with different colors indicating different nodal rings. Inset: Enlarged view of the bands around Γ point, where the four bands are identified as flexural Lamb (FL) modes, waterborne guided (WG) modes, shear horizontal (SH) modes, and extensional Lamb (EL) modes, respectively. **c** Distribution of the nodal rings in the FBZ. The colors of the nodal rings are the same as the corresponding dots in (b). **d** Spectral variations of the three nodal rings. **e** 3D band structures of the first two modes on specified cross sections of the FBZ. Nodal rings formed by their crossings are denoted.

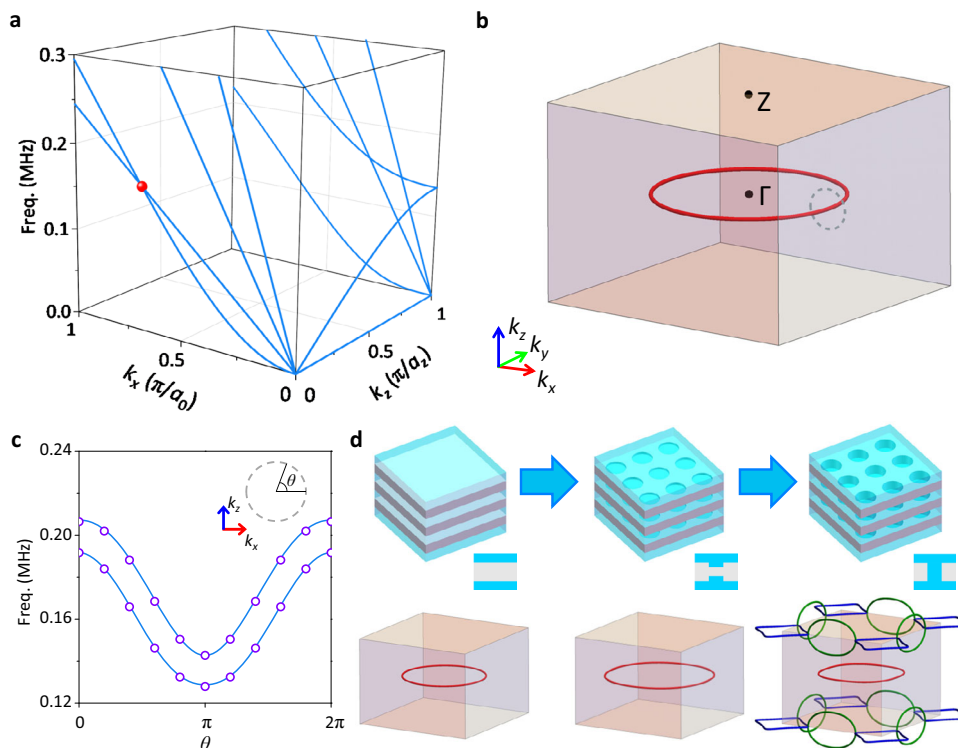


Fig. 2 | Origins and analysis of the nodal rings. **a** Band structure of periodic metallic plates without perforations. **b** Distribution of the ideal type-II nodal ring for (a). No other nodal rings exist. **c** Band structure on the dashed loop denoted in (b). The radius of the circular loop is $0.1\pi/a_0$. Solid lines and hollow dots respectively

denote the results from full-wave simulations and the effective Hamiltonian. **d** Evolution of the nodal rings, from uniform plates to plates with blind holes and finally through holes.

Brillouin zone (FBZ) features their emergence from zero frequency at Γ point. The 1st band intersects with the 2nd band on high-symmetry planes of the FBZ. Their touching points, as indicated by the red, blue, and green dots, form different nodal rings, respectively. Moreover, these touching points are all gapped slightly away from corresponding high-symmetry planes in the reciprocal space, which are the characteristics of nodal rings (see Supplementary Note 1). The calculated distribution of the nodal rings (Fig. 1c) in the FBZ further reveal that the blue and green nodal rings are chained together, forming nodal chains. Detailed shapes and frequency variances of the nodal rings are given (Fig. 1d). According to the band slopes around the nodal rings, the red and blue nodal rings are type-II nodal rings, while the green nodal rings are hybrid nodal rings (Fig. 1e). The hybrid green nodal rings have a relatively large frequency dispersion ($\Delta\omega/\omega_{\text{mid}} \sim 12.3\%$, with $\Delta\omega$ being the frequency variation and ω_{mid} being the middle of frequencies), while the type-II red and blue nodal rings have smaller frequency dispersions ($\Delta\omega/\omega_{\text{mid}} \sim 6.6\%$ and $\sim 1.4\%$ for the red and blue ones). Additional nodal rings may also appear between the 2nd and higher bands, but they are all inside the sound cone (bulk acoustic waves in water) when projected along the z direction, out of our interest.

Theoretical modeling of intrinsic dynamics

Notably, the nodal rings originate from the fluid-solid interaction, since transverse components of the plates' displacements cannot be ignored (see Supplementary Note 2). To clarify this point, we first consider band dispersions near Γ point (inset in Fig. 1(b)), around which the first four bands can be classified as the lowest-order water-borne guided (WG) mode and the three lowest-order plate modes; the flexure Lamb (FL) mode, the extensional Lamb (EL) mode, and the shear horizontal (SH) mode (see Supplementary Note 3 for their mode profiles near Γ point). The WG mode and FL mode have opposite parities with respect to the mirror symmetry M_z ($z \rightarrow -z$) and are decoupled when $k_z = 0$ (see Supplementary Note 15). Far away from

the Γ point, the hybridizations between these modes can be significant, so that the bands cannot be easily identified. To illuminate the emergence of the nodal rings, we consider the case that periodic metallic plates are arranged in the same manner but without any perforations. The calculated bands still feature the touching point between the 1st and 2nd bands on $k_z = 0$ plane (Fig. 2a). In this case, around Γ point with $k_z = 0$, we derive the dispersions based on the transfer matrix method (see Supplementary Note 9)

$$\begin{aligned} \omega_{\text{WG}} &= c_w k_r \\ \omega_{\text{FL}} &= \sqrt{\frac{D}{\rho_m t_m + \rho_w t_w}} k_r^2, \end{aligned} \quad (1)$$

where $k_r = \sqrt{k_x^2 + k_y^2}$, D and ρ_m are the bending stiffness and density of the plates, c_w and ρ_w are the sound speed and density of the background fluid (water). Therefore, in the long-wavelength limit, for the FL mode, a quadratic asymptotic behavior $\omega_{\text{FL}} \sim k_r^2$ is observed, which is similar to the case of flexural waves on a free-standing thin plate. In contrast, for the WG mode coinciding with sound cone, a typical linear asymptotic behavior $\omega_{\text{WG}} \sim k_r$ is observed. As they emerge together from Γ point when $k_z = 0$, they will eventually cross each other along a closed loop with both slopes positive, forming a type-II nodal ring (Fig. 2b). We note that this red nodal ring is rather robust against choices of material and geometric parameters (see Supplementary Note 8). It is also an ideal type-II nodal ring without frequency variation because the plates without perforations are rotation-invariant. We have derived an effective Hamiltonian for the red nodal ring using the transfer matrix method (see Supplementary Note 9),

$$H_{\text{eff}}(\mathbf{k}) = v_r(k_r - k_{r0})\sigma_3 + v_z k_z \sigma_1 + v_0(k_r - k_{r0})\sigma_0, \quad (2)$$

where k_{r0} is the radius of the nodal ring, σ_i ($i = 1, 2, 3$) are Pauli matrices, σ_0 is 2×2 identity matrix, and v_0 , v_r , v_z are fitted velocity parameters,

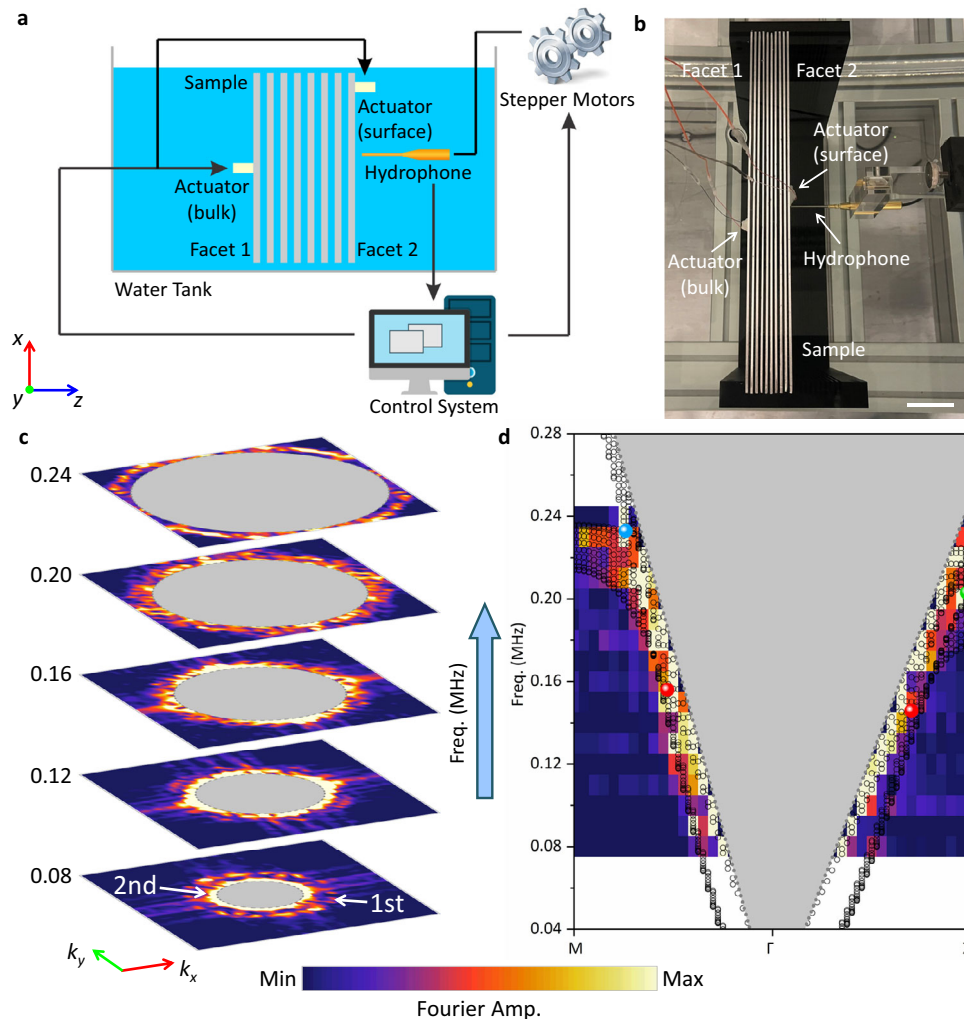


Fig. 3 | Experimental observation of type-II nodal rings. **a** Schematic of experimental setup for near-field scanning. A hydrophone is employed to image the ultrasound signal at facet 2. Piezoelectric actuators are used to actuate the phononic crystal. When detecting bulk bands, the actuator attached on facet 1 is excited, while detecting the surface states, the actuator attached on facet 2 is excited. **b** Photograph of the sample and experimental setup. White scale bar: 40 mm. **c** Spatial Fourier spectra of experimentally imaged fields at corresponding

frequencies. The bright stripes correspond to modes of the 1st and 2nd bands excited and observed in experiments. Gray-shaded regions: the sound cone projected on the k_x - k_y plane. **d** Experimental Fourier spectra along high-symmetry directions. Gray shaded region: the projected sound cone. Black circles: calculated band structure projected along k_x . The bright stripes correspond to excited modes, which generally overlap with black circles from full-wave simulations. The colored dots represent the nodal rings of the same color denoted in Fig. 1.

with $|v_o/v_r| > 1$ manifested by the strong tilting of the two bands. On a closed loop encircling the type-II nodal ring, the bands obtained by solving the effective Hamiltonian of Eq. (2) agree excellently with those from full-wave simulations (Fig. 2c), further validating the analysis.

After a square lattice of perforations are introduced, the blue and green nodal rings emerge, while the red nodal ring is slightly distorted due to the breaking of rotation-invariance. Distinct from the robust red nodal rings associated with the plate thickness (see Supplementary Note 4), we note that the green and blue nodal rings are directly related to the through holes. To illustrate this point, instead of through holes, we also evaluate the case of blind holes on two sides of the metallic plates, with the limiting case that they perforate the metallic plates (see Supplementary Note 5). The evolution of the band structure reveals that only the red nodal ring, arising solely from the fluid-solid interaction (see Supplementary Note 16), can exist with blind holes (Fig. 2d). The green nodal rings could shrink (expand) in company with the expanding (shrinking) blue nodal rings as they are chained together⁴² due to the mirror symmetries M_x ($x \rightarrow -x$) and M_y ($y \rightarrow -y$). The blue nodal rings will reconnect if they touch each other when we tune geometric parameters and consequently the green nodal rings will be

eliminated (see Supplementary Note 6). The blue and green nodal rings are largely owing to the acoustic resonance mode of the through holes (see Supplementary Note 17). Nevertheless, all the nodal rings are protected by corresponding mirror symmetries. They will all be gapped if there are no mirror symmetries in the phononic crystal (see Supplementary Note 7). Further, interface states of topological origin can be constructed by combining the phononic crystals that break the mirror symmetry in different ways⁴³ (see Supplementary Note 18).

Experimental observation of type-II nodal rings

Next, we perform ultrasonic near-field scanning in water to experimentally validate the type-II nodal rings⁴⁴. When probing bulk bands with the experiment setup (Fig. 3a, see Methods for details), out-of-plane displacement, which couples efficiently with underwater ultrasound, is generated by a piezoelectric actuator. The actuator is attached on one side (x - y surface) of the sample, and the ultrasound field on the opposite side is detected point-by-point (Fig. 3b). The imaged fields are then Fourier transformed⁴⁴ to extract the intensity spectra outside the sound cone in the reciprocal space (surface FBZ). The bright stripes in the intensity spectra indicate excited bulk modes

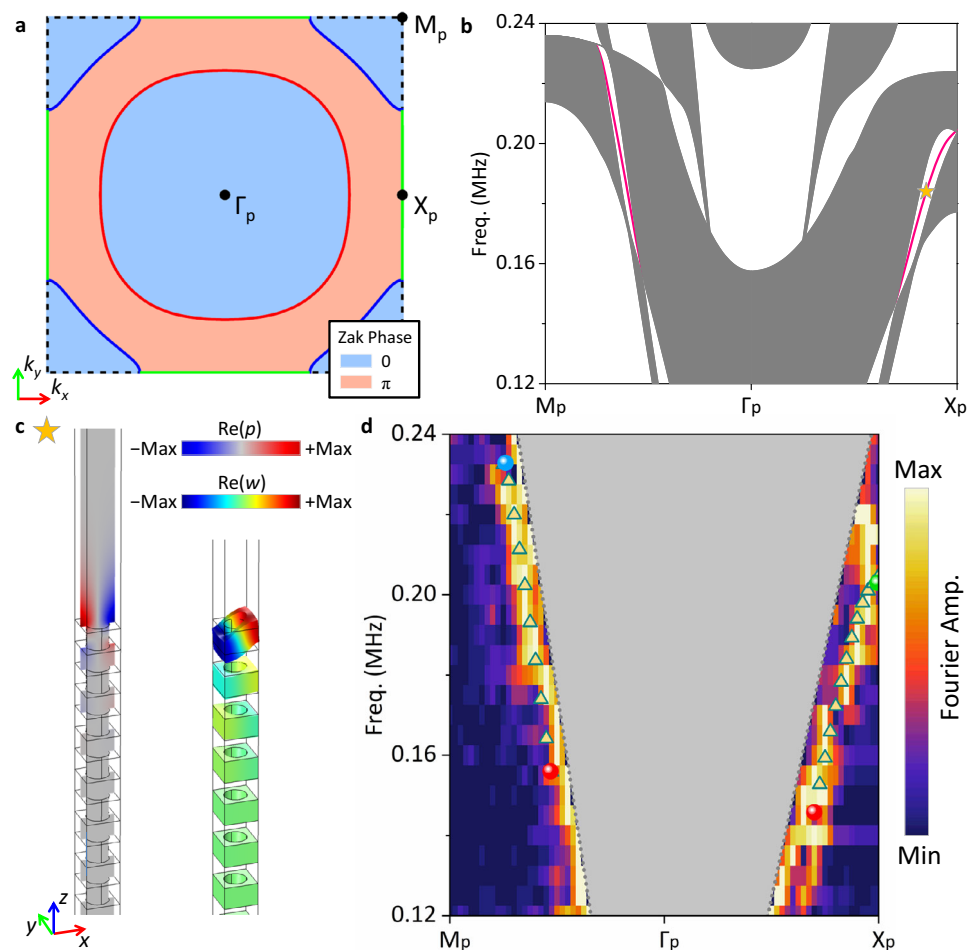


Fig. 4 | Strongly tilted drumhead surface state (DSS) between nodal rings. **a** Distribution of Zak phase on the surface FBZ projected along z direction. **b** Calculated projected band structure of a supercell terminated by x - y surface. Solid lines represent the strongly tilted DSS. Gray shaded regions denote the projected bulk bands. **c** Calculated field maps of acoustic pressure ($\text{Re}(p)$) and elastic

displacements ($\text{Re}(u)$, $\text{Re}(v)$, $\text{Re}(w)$) for the marked point in **(b)**. The thin solid lines outline profile of the supercell without elastic displacements. **d** Experimental Fourier spectra along high-symmetry directions when exciting and detecting the ultrasound at the same side of the phononic crystal. Triangle scatters: the calculated dispersion of the strongly tilted DSS along the high-symmetry directions.

outside sound cone in experiments that is projected over k_z , and their evolution with respect to frequency is presented (Fig. 3c). For better corroboration, we extract spatial Fourier spectra along high symmetry directions, and the occupied ranges of excited modes in surface FBZ also agree quite well with the calculated band structure projected over k_z (Fig. 3d). For further confirmation, we have carried out control experiments with in-plane lattice constant changed to $a_0 = 4$ mm, and the results also agree with corresponding simulations (see Supplementary Note 20).

Emergence of strongly tilted drumhead surface states

To further elaborate the topological effects of type-II nodal rings, we also note the existence of drumhead surface state (DSS) between the red type-II nodal ring on $k_z = 0$ and the blue type-II nodal ring on $k_z = \pm\pi/a_z$. The DSS is closely related to the Zak phase along k_z direction that is quantized owing to the mirror symmetry M_z ($z \rightarrow -z$) of the phononic crystal. The distribution of the Zak phase in the surface FBZ (Fig. 4a) is delineated by the projection of the two nodal rings on k_x - k_y plane⁴⁵ (see Supplementary Note 10 for numerical verifications), and it suggests possible existence of DSS in the region with Zak phase¹² equal to π . The calculated projected band structure of a supercell terminated by its x - y surface confirms that a strongly tilted DSS emerges in the partial bandgap (Fig. 4b), a hallmark of the topological effect of the type-II nodal rings. This strong tilting is in sharp contrast to DSSs of

type-I nodal rings, where they are generally flat. The calculated 3D dispersion of the DSS also demonstrates its strong tilting (see Supplementary Note 11). The field maps of the strongly tilted DSS (Fig. 4c), including both acoustic pressure and out-of-plane displacement, attests that the state is indeed localized on the surface of the phononic crystal, and is a hybridized mode with significant energy distributed in both water and plates (see Supplementary Note 12).

Finally, we seek to experimentally detect the strongly tilted DSS. Based on the essentially same experimental setup but the source and detector now on the same x - y side (Fig. 3(a)), we perform near-field scanning and the imaged fields (see Supplementary Note 13) are then Fourier transformed again. The excited modes revealed in the experimentally extracted Fourier spectra (Fig. 4d) reach good agreement with numerical calculations, thereby confirming the existence of the DSS along with its key signature, the strong tilting. Because we cannot prevent the excitation of bulk states, there are also bright stripes emerging at low-frequency range (see Supplementary Note 19). Control experiments are also carried out to further confirm our findings (see Supplementary Note 20).

Discussion

In this work, we demonstrate an approach for topological phononics and with the approach, we realize type-II nodal rings in a phononic crystal, and experimentally capture the associated key topological

phenomena with underwater ultrasound. The simple phononic crystal, only needing perforation during manufacturing, can be directly rescaled to higher frequency regimes. It may inspire on-chip devices with its propagating topological surface waves (strongly tilted DSSs). Generally, our approach reveals that for sound in fluids and solids, the interaction between their fundamentally different wave dynamics contains rich topological physics, with designs guided by the symmetry. For example, the type-II nodal rings can be gapped into ideal type-II Weyl points^{13,35} by lowering the symmetry of the phononic crystal (see Supplementary Note 14), and hence our findings expand topological systems and can serve as platforms to explore topological physics in a much simpler manner, not to mention the significantly reduced thermo-viscous losses of sound in water compared with air⁴⁶. Remarkably, the rich physics discovered in this platform may also advance theoretical studies and experimental realizations of other nodal-line topologies, such as non-Abelian nodal links³¹ and topological charges⁴⁷.

Methods

Simulations

In all simulations, the finite-element method software COMSOL Multiphysics is employed. The aluminum is modeled with density $\rho_m = 2700 \text{ kg/m}^3$, Young's modulus $E = 69 \text{ GPa}$, and Poisson's ratio $\nu = 0.33$, while the water is modeled with $\rho_w = 1000 \text{ kg/m}^3$ and speed of sound $c_w = 1490 \text{ m/s}$. When calculating bulk band structures using a unit cell, periodic boundary conditions are applied on all boundaries. When calculating projected band structures using a supercell, periodic boundary conditions are applied on periodic boundaries and plane-wave radiation boundary conditions are applied on terminated boundaries to model finite structures. The terminated boundaries are five lattice constants away from finite structures, which proves to be appropriate as the modes of interest are evanescent along the z (out-of-plane) direction outside the structures. The maximum element size of the meshes in all simulations is 0.5 mm , which is $\sim 1/10$ of the wavelength of underwater ultrasound at 0.30 MHz .

Experiments

The aluminum plates (pure aluminum) are perforated using a sheet metal punching machine and installed on a frame. Piezoelectric actuators (KEMET, USA) are attached on the outside facets of the aluminum plates as the source in experiments. A needle hydrophone mounted on a 3D motorized stage is used as the detector to collect the ultrasound data and perform near-field scanning. Signal of each frequency is emitted to excite the actuator, and corresponding time-domain signals are collected point-by-point using the hydrophone. The time-domain signals are Fourier transformed to obtain the field maps in the real space for each frequency. We then perform spatial Fourier transforms to retrieve band structures in the reciprocal space. The step resolution of scanning is $1 \text{ mm} \times 1 \text{ mm}$.

Data availability

The data which support the figures and other findings within this paper are available from the corresponding authors upon request.

References

- Qi, X.-L. & Zhang, S.-C. Topological insulators and superconductors. *Rev. Mod. Phys.* **83**, 1057 (2011).
- Wieder, B. J. et al. Topological materials discovery from crystal symmetry. *Nat. Rev. Mater.* 1–21 (2021).
- Ozawa, T. et al. Topological photonics. *Rev. Mod. Phys.* **91**, 015006 (2019).
- Ma, G., Xiao, M. & Chan, C. T. Topological phases in acoustic and mechanical systems. *Nat. Rev. Phys.* **1**, 281–294 (2019).
- Hafezi, M., Mittal, S., Fan, J., Migdall, A. & Taylor, J. Imaging topological edge states in silicon photonics. *Nat. Photonics* **7**, 1001–1005 (2013).
- Yang, Y. et al. Realization of a three-dimensional photonic topological insulator. *Nature* **565**, 622–626 (2019).
- He, C. et al. Acoustic topological insulator and robust one-way sound transport. *Nat. Phys.*, <https://doi.org/10.1038/nphys3867> (2015).
- Miniaci, M., Pal, R., Morvan, B. & Ruzzene, M. Experimental observation of topologically protected helical edge modes in patterned elastic plates. *Phys. Rev. X* **8**, 031074 (2018).
- Li, F., Huang, X., Lu, J., Ma, J. & Liu, Z. Weyl points and Fermi arcs in a chiral phononic crystal. *Nat. Phys.* **14**, 30 (2018).
- He, H. et al. Topological negative refraction of surface acoustic waves in a Weyl phononic crystal. *Nature* **560**, 61–64 (2018).
- Xie, B. et al. Experimental Realization of Type-II Weyl Points and Fermi Arcs in Phononic Crystal. *Phys. Rev. Lett.* **122**, 104302 (2019).
- Deng, W. et al. Nodal rings and drumhead surface states in phononic crystals. *Nat. Commun.* **10**, 1769 (2019).
- Huang, X., Deng, W., Li, F., Lu, J. & Liu, Z. Ideal type-II Weyl phase and topological transition in phononic crystals. *Phys. Rev. Lett.* **124**, 206802 (2020).
- Wu, X. et al. Deterministic Scheme for Two-Dimensional Type-II Dirac Points and Experimental Realization in Acoustics. *Phys. Rev. Lett.* **124**, 075501 (2020).
- Bahari, B. et al. Nonreciprocal lasing in topological cavities of arbitrary geometries. *Science* **358**, 636–640 (2017).
- Bandres, M. A. et al. Topological insulator laser: Experiments. *Science* **359**, eaar4005 (2018).
- Budich, J. C. & Bergholtz, E. J. Non-Hermitian topological sensors. *Phys. Rev. Lett.* **125**, 180403 (2020).
- Zangeneh-Nejad, F. & Fleury, R. Topological fano resonances. *Phys. Rev. Lett.* **122**, 014301 (2019).
- Weidemann, S. et al. Topological funneling of light. *Science* **368**, 311–314 (2020).
- Wen, Z. et al. Topological cavities in phononic plates for robust energy harvesting. *Mech. Syst. Signal Process.* **162**, 108047 (2022).
- Cummer, S. A., Christensen, J. & Alù, A. Controlling sound with acoustic metamaterials. *Nat. Rev. Mater.* **1**, 16001 (2016).
- Watanabe, H. & Lu, L. Space group theory of photonic bands. *Phys. Rev. Lett.* **121**, 263903 (2018).
- Fan, X. et al. Probing Weyl Physics with One-Dimensional Sonic Crystals. *Phys. Rev. Lett.* **122**, 136802 (2019).
- Shen, Y. et al. Valley-projected edge modes observed in underwater sonic crystals. *Appl. Phys. Lett.* **114**, 023501 (2019).
- Novoselov, K. S. et al. Two-dimensional gas of massless Dirac fermions in graphene. *Nature* **438**, 197 (2005).
- Lu, L. et al. Experimental observation of Weyl points. *Science* **349**, 622–624 (2015).
- Mullen, K., Uchoa, B. & Glatzhofer, D. T. Line of Dirac nodes in hyperhoneycomb lattices. *Phys. Rev. Lett.* **115**, 026403 (2015).
- Fang, C., Chen, Y., Kee, H.-Y. & Fu, L. Topological nodal line semimetals with and without spin-orbital coupling. *Phys. Rev. B* **92**, 081201 (2015).
- Gao, W. et al. Experimental observation of photonic nodal line degeneracies in metacrystals. *Nat. Commun.* **9**, 950 (2018).
- Yan, Q. et al. Experimental discovery of nodal chains. *Nat. Phys.* **14**, 461 (2018).
- Yang, E. et al. Observation of non-Abelian nodal links in photonics. *Phys. Rev. Lett.* **125**, 033901 (2020).
- Soluyanov, A. A. et al. Type-II Weyl semimetals. *Nature* **527**, 495 (2015).

33. Xu, S.-Y. et al. Discovery of Lorentz-violating type II Weyl fermions in LaAlGe. *Sci. Adv.* **3**, e1603266 (2017).
34. Hu, C. et al. Type-II Dirac Photons at Metasurfaces. *Phys. Rev. Lett.* **121**, 024301 (2018).
35. Xia, B., Wang, R., Chen, Z., Zhao, Y. & Xu, H. Symmetry-Protected Ideal Type-II Weyl Phonons in CdTe. *Phys. Rev. Lett.* **123**, 065501 (2019).
36. Deng, K. et al. Experimental observation of topological Fermi arcs in type-II Weyl semimetal MoTe₂. *Nat. Phys.* **12**, 1105 (2016).
37. Li, S. et al. Type-II nodal loops: Theory and material realization. *Phys. Rev. B* **96**, 081106 (2017).
38. Chang, T. R. et al. Realization of a type-II nodal-line semimetal in Mg₃Bi₂. *Adv. Sci.* **6**, 1800897 (2019).
39. Real, B. et al. Semi-Dirac transport and anisotropic localization in polariton honeycomb lattices. *Phys. Rev. Lett.* **125**, 186601 (2020).
40. Ma, J. et al. Nonlinear photoresponse of type-II Weyl semimetals. *Nat. Mater.* **18**, 476–481 (2019).
41. Yang, Z. & Zhang, B. Acoustic Type-II Weyl Nodes from Stacking Dimerized Chains. *Phys. Rev. Lett.* **117**, 224301 (2016).
42. Wu, Q., Soluyanov, A. A. & Bzdušek, T. Non-Abelian band topology in noninteracting metals. *Science* **365**, 1273–1277 (2019).
43. Yang, B. et al. Momentum space toroidal moment in a photonic metamaterial. *Nat. Commun.* **12**, 1784 (2021).
44. Estrada, H. et al. Engineering surface waves in flat phononic plates. *Phys. Rev. B* **85**, 174301 (2012).
45. Hirayama, M., Okugawa, R., Miyake, T. & Murakami, S. Topological Dirac nodal lines and surface charges in fcc alkaline earth metals. *Nat. Commun.* **8**, 14022 (2017).
46. Mousavi, S. H., Khanikaev, A. B. & Wang, Z. Topologically protected elastic waves in phononic metamaterials. *Nat. Commun.* **6**, 8682 (2015).
47. Guo, Q. et al. Experimental observation of non-Abelian topological charges and edge states. *Nature* **594**, 195–200 (2021).

Acknowledgements

This work is supported by grants from Hong Kong Research Grants Council (Grant Nos. C6013-18G, AoE/P-502/20, 15205219) and National Natural Science Foundation of China (Grant Nos. 11774297, 12104383). T. Liu also acknowledges supports from Research Grants Council (Grant No. PolyU 15219221) and Internal Research Fund of The Hong Kong Polytechnic University (Grant No. ZZLC).

Author contributions

X.W. and X.Z. conceived the original idea. X.W. performed the simulations. X.W. and R.-Y.Z. derived the theory. H.F., T.L., and Z.G. carried out the experiments. X.Z. and J.Z. supervised the project. All authors contributed to scientific discussions of the manuscript.

Competing interests

The authors declare no competing interests.

Additional information

Supplementary information The online version contains supplementary material available at <https://doi.org/10.1038/s41467-022-33896-4>.

Correspondence and requests for materials should be addressed to Jie Zhu or Xiang Zhang.

Peer review information *Nature Communications* thanks the other anonymous reviewer(s) for their contribution to the peer review of this work.

Reprints and permission information is available at <http://www.nature.com/reprints>

Publisher's note Springer Nature remains neutral with regard to jurisdictional claims in published maps and institutional affiliations.

Open Access This article is licensed under a Creative Commons Attribution 4.0 International License, which permits use, sharing, adaptation, distribution and reproduction in any medium or format, as long as you give appropriate credit to the original author(s) and the source, provide a link to the Creative Commons license, and indicate if changes were made. The images or other third party material in this article are included in the article's Creative Commons license, unless indicated otherwise in a credit line to the material. If material is not included in the article's Creative Commons license and your intended use is not permitted by statutory regulation or exceeds the permitted use, you will need to obtain permission directly from the copyright holder. To view a copy of this license, visit <http://creativecommons.org/licenses/by/4.0/>.

© The Author(s) 2022